



# $^{29}\text{Si}$ solid state MAS NMR study on leaching behaviors and chemical stability of different Mg-silicate structures for $\text{CO}_2$ sequestration

Guanhe Rim<sup>a,b</sup>, Ariane Katrina Marchese<sup>d</sup>, Phillip Stallworth<sup>d</sup>, Steven G. Greenbaum<sup>d</sup>, Ah-Hyung Alissa Park<sup>a,b,c,\*</sup>

<sup>a</sup> Department of Earth and Environmental Engineering, Columbia University, New York, NY 10027, USA

<sup>b</sup> Lenfest Center for Sustainable Energy, The Earth Institute, New York, NY 10027, USA

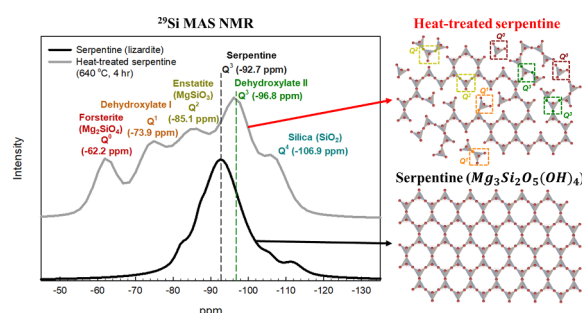
<sup>c</sup> Department of Chemical Engineering, Columbia University, New York, NY 10027, USA

<sup>d</sup> Department of Physics & Astronomy, Hunter College of the City University of New York, New York, NY 10065, USA

## HIGHLIGHTS

- Dissolution mechanisms of heat-treated serpentine were studied by  $^{29}\text{Si}$  MAS NMR.
- Chemical stabilities of different silicate structures ( $\text{Q}^0$ – $\text{Q}^4$ ) were determined.
- The amorphous  $\text{Q}^1$  and  $\text{Q}^2$  structures were most reactive in carbonic acid.
- This study identified different reaction pathways for  $\text{CO}_2$  sequestration.

## GRAPHICAL ABSTRACT



## ARTICLE INFO

### Keywords:

Carbon mineralization  
Silicate  
 $^{29}\text{Si}$  MAS NMR  
Leaching behaviors  
Heat treatment

## ABSTRACT

Silicon is one of the most earth abundant elements, and thus, the fate and reactivity of silicate materials are often important for various energy and environmental technologies including carbon sequestration, where  $\text{CO}_2$  is captured and stored as a thermodynamically stable solid carbonate phase. Thus, understanding the structures and chemistries of different silicate phases has become an important research aim. In this study, the changes in the silicate structures ( $\text{Q}^0$ – $\text{Q}^4$ ) of heat-treated Mg-bearing mineral (serpentine) exposed to a  $\text{CO}_2$ -water system (carbonic acid) was investigated using  $^{29}\text{Si}$  MAS NMR, XRPD and ICP-OES and the identified structures were employed to explain complex leaching behaviors of silicate materials. The  $^{29}\text{Si}$  MAS NMR and XRPD analysis indicated that the heat-treated serpentine is a mixture of amorphous ( $\text{Q}^1$ : dehydroxylate I,  $\text{Q}^2$ : enstatite,  $\text{Q}^4$ : silica) and crystalline ( $\text{Q}^0$ : forsterite,  $\text{Q}^3$ : dehydroxylate II and serpentine) phase, while natural serpentine mineral has single crystalline  $\text{Q}^3$  silicate structure. The leaching experiments showed that both Mg and Si in the amorphous silicate structures ( $\text{Q}^1$ : dehydroxylate I,  $\text{Q}^2$ : enstatite) are more soluble than those in crystalline phase ( $\text{Q}^0$ : forsterite,  $\text{Q}^3$ : dehydroxylate II and serpentine). Therefore, tuning the silicate structure towards  $\text{Q}^1$  and  $\text{Q}^2$  would significantly improve carbon sequestration potential of silicate minerals, whereas silicate materials with  $\text{Q}^3$  structure would provide great chemical stabilities in acidic conditions. The solubilities of silicate structures were in the order of  $\text{Q}^1$  (dehydroxylate I) >  $\text{Q}^2$  (enstatite) >  $\text{Q}^0$  (forsterite) >  $\text{Q}^3$  (dehydroxylate II) >  $\text{Q}^3$  (serpentine) and this finding can be used to better design a wide range of energy and environmental materials and reaction systems.

\* Corresponding author at: Department of Earth and Environmental Engineering and Department of Chemical Engineering, Columbia University, New York, NY 10027, USA.

E-mail address: [ap2622@columbia.edu](mailto:ap2622@columbia.edu) (A.-H.A. Park).

<https://doi.org/10.1016/j.cej.2020.125204>

Received 22 January 2020; Received in revised form 20 April 2020; Accepted 22 April 2020

Available online 25 April 2020

1385-8947/ © 2020 Elsevier B.V. All rights reserved.

## 1. Introduction

Since the industrial revolution, the atmospheric  $\text{CO}_2$  concentration has steadily increased due to the combustion of fossil fuels, reaching 410 ppm in September 2019 [1]. Researchers have correlated the intensification of climate change with the increase of atmospheric  $\text{CO}_2$  concentration [2]. According to the 2018 IPCC report [3], it was recognized that the anthropogenic greenhouse gas emissions caused by human activities are major drivers for global warming of  $1.0^\circ\text{C}$  above the pre-industrial level. With the continued reliance on fossil fuels in various parts of the world, atmospheric  $\text{CO}_2$  is likely to further increase, resulting in  $1.5^\circ\text{C}$  of global warming between 2030 and 2052 with long-term changes in climate-related natural systems, such as sea level rise [3]. The natural carbon cycle process can potentially slow down the increase rate of atmospheric  $\text{CO}_2$  concentration [4], but engineered solutions are also needed to reduce  $\text{CO}_2$  emissions. Due to its unprecedented scale, the mitigation of climate change requires a wide range of multifaceted solutions. The Mission Innovation lists the following eight innovation challenges to encourage the global efforts to accelerate the research and development in addressing climate change mitigation: (1) smart grid, (2) off-grid access to electricity, (3) carbon capture, (4) sustainable biofuels, (5) converting sunlight, (6) clean energy materials, (7) affordable heating and cooling of buildings, and (8) renewable and clean hydrogen [5,6]. In particular, we have been focusing on the development of novel materials and separation and reaction pathways for Carbon Capture, Utilization and Storage (CCUS) and energy storage technologies.

When developing CCUS or energy storage (e.g., novel electrolytes for batteries) technologies, materials selection is very important since the availabilities of natural resources and their engineered forms are keys to develop large-scale energy and environmental technologies. Silicon is the second most abundant element in the Earth's crust (about 28 wt%) next to oxygen and they mostly exist as silicate minerals forming > 90% of the Earth crust [7]. Thus, as shown in Fig. 1, the study of various silicate materials in terms of their structures and reactivities has become one of the most important fundamental studies for sustainable energy and environmental research.

For example, carbon mineralization, which converts  $\text{CO}_2$  to thermodynamically stable solid carbonate form is one of emerging CCUS technologies with long-term stability. The carbon mineralization

scheme was proposed by Seifritz [8] as an alternative approach to sequester  $\text{CO}_2$  in geologic formations. This is a chemically enhanced form of the natural weathering process between natural silicate minerals and  $\text{CO}_2$ . Earth abundant minerals including serpentine ( $\text{Mg}_3\text{Si}_2\text{O}_5(\text{OH})_4$ ) are estimated to have a  $\text{CO}_2$  sequestration potential over 10,000 Gt C [9,10]. The overall reaction produces a long-lived metal-carbonate phase via a thermodynamically favorable reaction pathway [5,11]. If the carbon mineralization process is performed in an engineered reactor system, high-purity products, such as green construction materials and high surface area silica, can be produced with tailored chemical and physical properties while sequestering  $\text{CO}_2$ . Currently, the global construction materials market is tremendous (> 50 billion tons produced annually) [11] and a recent market assessment estimated that the carbonate-based construction materials may have the potential to utilize 3–6 Gt of  $\text{CO}_2$  with annual revenues of \$1 trillion by 2030 [5,12]. Carbon mineralization can also be performed using alkaline industrial wastes (e.g., steel slag and cement kiln dust) [11]. Thus, carbon mineralization is considered to be the most energy-efficient and economical CCUS pathway with multiple environmental benefits at this time [11].

$\text{CO}_2$  reaction with silicate minerals is quite complex since many silicate structures exist depending on the reactive environments. For instance, earth abundant Mg-bearing mineral, serpentine ( $\text{Mg}_3\text{Si}_2\text{O}_5(\text{OH})_4$ ), consists of 1:1 alternatively stacked tetrahedral (silica-like) and octahedral (brucite-like) sheets and it can react with  $\text{CO}_2$  via following steps: (i)  $\text{Mg}^{2+}$  extraction from the silicate structure in aqueous phase by acid (ion exchange between  $\text{Mg}^{2+}$  and  $\text{H}^+$ ), and (ii) precipitation reaction between extracted  $\text{Mg}^{2+}_{(\text{aq})}$  and dissolved carbon dioxide ( $\text{CO}_3^{2-}_{(\text{aq})}$ ) forming solid  $\text{MgCO}_3_{(\text{s})}$  phases. The main kinetic barrier for carbon sequestration with Mg-silicate minerals (e.g., serpentine) is considered to be the mineral dissolution step because of the low reactivity of natural silicate minerals [13]. A number of studies have focused on the activation of serpentine via heat-treatment that effectively alters the silicate structures to increase the leaching rate of Mg and other metals from silicate minerals [14–23].

Most silicate minerals consist of  $\text{SiO}_4$  tetrahedra, which may exist as isolated structures or interconnected complicated structures [24]. The way the  $\text{SiO}_4$  tetrahedra structures are linked determines the overall mineral structures. Thus, silicate minerals are generally classified based on the degree of polymerization of  $\text{SiO}_4$  and denoted as symbol  $\text{Q}^n$

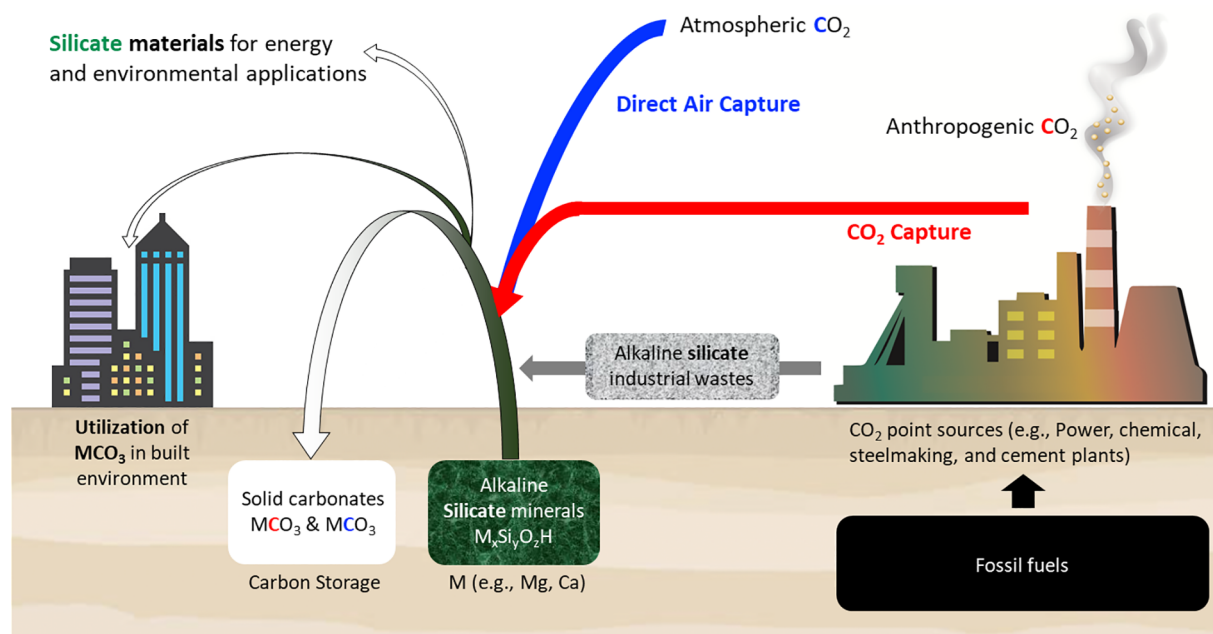


Fig. 1. Flows of C and Si-bearing materials in the Earth and engineered energy and environmental systems.

( $n = 0, 1, 2, 3, 4$ ), where  $n$  is the number of shared oxygens that “bridge” silicon in other  $\text{SiO}_4$  tetrahedra. When the serpentine silicate structure (predominantly  $\text{Q}^3$ ) is heated above  $600^\circ\text{C}$ , the chemically bonded hydroxyl group (OH) is expelled, leading to structural disorder and the formation of new silicate structures ( $\text{Q}^0$ ,  $\text{Q}^1$ ,  $\text{Q}^2$ ,  $\text{Q}^4$  and altered  $\text{Q}^3$ ) with an increase in reactive surface [25–30]. More complex silicate structures are formed with increased reactivity after the heat treatment of serpentine.

While the thermal decomposition (dehydroxylation) of serpentine minerals have been investigated by a number of studies [25,27,29,30,32–42], there are very limited studies available on the changes in the silicate structures during the dissolution of heat-treated serpentine. Compared to previously studied natural silicate minerals, heat-treated serpentine has more complex silicate structures, and thus, understanding leaching behaviors and chemical stability of these silicate minerals would provide valuable insights into how various Si-based materials can be used in energy and environmental systems.  $^{29}\text{Si}$  MAS NMR is a well-established solid analysis technique to investigate various silicate structures, and thus, it is selected to investigate the dissolution mechanisms of heat-treated serpentine in terms of the  $^{29}\text{Si}$  chemical shift for different Si in  $\text{SiO}_4$  tetrahedral coordination (see Fig. 2). As shown in Table 1, many previous studies used this technique to determine the various silicate structures and reported their  $^{29}\text{Si}$  chemical shift. However, limited  $^{29}\text{Si}$  chemical shift data for the heat-treatment of natural silicate minerals [29,40] and single-step carbon mineralization processes involving natural silicate minerals [43–47] were found in the literature.

In this study, a series of spectroscopic tools including  $^{29}\text{Si}$  solid state Magic Angle Spinning Nuclear Magnetic Resonance (MAS NMR), X-ray Powder Diffraction (XRPD) and Inductively Coupled Plasma Optical Emission Spectroscopy (ICP-OES) were employed to investigate the mineralogical and chemical changes within the heat-treated silicate mineral when it was subjected to a weak acid solution created by bubbling  $\text{CO}_2$  into water (carbonic acid). The dissolution behaviors of silicate materials are complex and influenced by many factors including mineralogy, morphology, particle size, solvent pH, reaction temperature, and partial pressure of  $\text{CO}_2$ . The experimental conditions of this study were carefully controlled so that the isolated effect of silicate structures on carbon mineralization can be investigated. The identified silicate structures ( $\text{Q}^0 - \text{Q}^4$ ) were used to provide insights into how Mg was liberated from different silicate structures in a carbonic acid environment. It is anticipated that the findings from this study will be able to not only provide a greater understanding of carbon mineralization reaction that fixes gaseous  $\text{CO}_2$  into thermodynamically stable carbonate phases but also provide insights into how Si-based materials can be used in different chemical environments, particularly acidic conditions.

## 2. Experimental

### 2.1. Dissolution experiments and solid sample collection

Heat-treated serpentine (HTS) was obtained from the collaborating Australian-based company, Mineral Carbonation International (MCI). The HTS was prepared by thermally treating natural lizardite mineral (serpentine) at  $640^\circ\text{C}$  for 4 hr. HTS sample was found to contain 23.2 wt% of Mg and 20.5 wt% of Si, and HTS particles smaller than  $100\ \mu\text{m}$  were used for this study to perform leaching experiments.

The first sets of experiments were carried out by exposing HTS sample to distilled water saturated with 1 atm  $\text{CO}_2$  at  $30^\circ\text{C}$ . The HTS slurry was mixed at 400 rpm for up to 240 min in a semi-batch reactor shown in Fig. 3. The pure  $\text{CO}_2$  gas was continuously bubbled into the HTS slurry at a constant flow rate of 1 L/min for the entire duration of the dissolution experiment. In order to investigate Mg and Si leaching behaviors under far-from-equilibrium and near-equilibrium conditions, two different slurry densities (SD) were selected: 0.1 and 5 wt%, respectively. This fresh HTS dissolution experiment was denoted as the

“First leaching.” For the 0.1 wt% slurry density case, two sets of solid residues were collected: one after 15 min and the other after 240 min reaction time and they were marked as HTS residue-I(a) and HTS residue-I(b), respectively. The solid residue produced after 240 min dissolution of 5 wt% HTS slurry was denoted as HTS residue-I(c).

The dissolution occurring during the “First leaching” step would have created different silicate structures, and thus, the second set of leaching experiments were performed using HTS residue-I(c) obtained from “First leaching” in order to investigate the Mg and Si leaching behaviors of different silicate phases. These experiments were noted as “Secondary leaching” and the experimental procedure was kept the same as before (i.e., 5 wt% of SD,  $30^\circ\text{C}$ ). The solid dissolution residue from “First leaching,” HTS residue-I(c), was introduced to a fresh distilled water saturated with  $\text{CO}_2$  and dissolved for 240 min. The solid sample was collected at the end of the dissolution experiment and marked as HTS residue-II(a).

In addition to the above described “Secondary leaching” experiments, two additional sets of experiments were performed to physically and chemically enhance the silicate mineral dissolution. The physical activation was performed with an internal grinding system in which the 5 wt% HTS residue-I(c) slurry was mixed with 20 vol% of 2.25 mm zirconia beads during the “Secondary leaching” to reduce/remove the passivation layer that may hinder the Mg and Si leaching from the mineral surface. By directly introducing the grinding media into the dissolution reactor with a relatively low slurry density, the energy required for the physical activation can be kept relatively small. The solid residue recovered from the internal grinding experiment was denoted as HTS residue-II(b).

Next, a combination of internal grinding and Mg-targeting ligand was tested for the dissolution behavior of HTS residue-I(c). 0.1 M of Na-citrate solution was introduced as the solvent instead of distilled water and the 5 wt% HTS residue-I(c) slurry mixed with 20 vol% 2.25 mm zirconia beads was reacted at  $30^\circ\text{C}$  for 240 min while bubbling  $\text{CO}_2$ . The solid residue obtained from this experiment was named as HTS residue-II(c).

Finally, in order to expose all the silicate phases to an extreme a leaching condition (i.e., strong acidic solvent) and determine their chemical stabilities, HTS residue-II(b), which was collected after the “Secondary leaching” with physical activation, was further treated using 2 M  $\text{HNO}_3$  solution at  $25^\circ\text{C}$ . A low slurry density of 0.5 wt% was used and the dissolution experiment was performed while agitating the mixture at 400 rpm for 6 hr 30 min to maximize the Mg extraction from

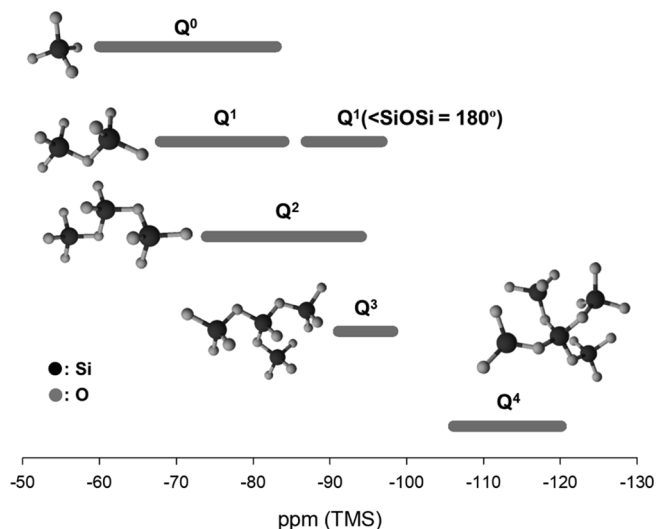
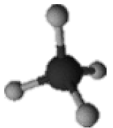
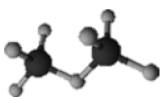
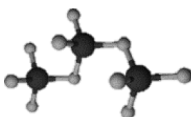
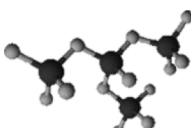
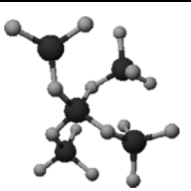
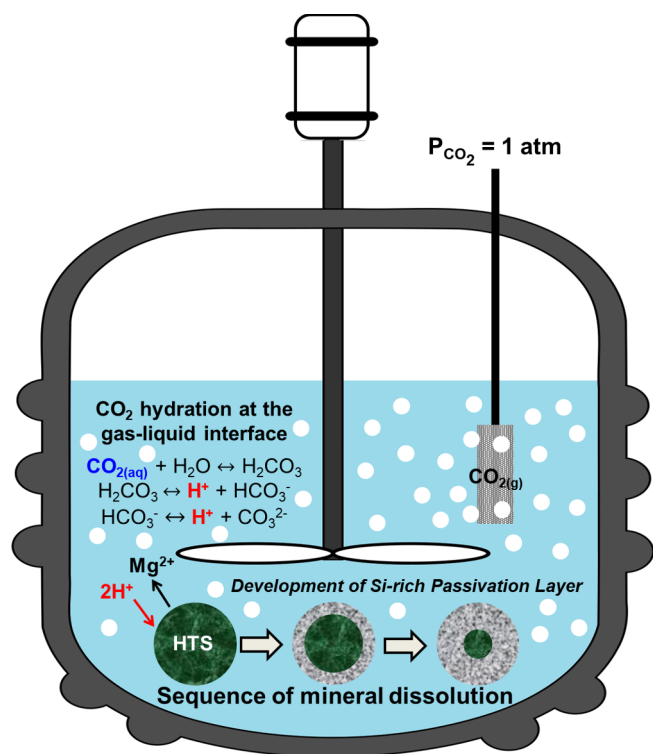


Fig. 2. Classification of silicate minerals according to the degree of polymerization of  $\text{SiO}_4$  and their chemical shifts in  $^{29}\text{Si}$  NMR (adapted from Magi et al. [31]).

**Table 1**  
<sup>29</sup>Si chemical shifts of various silicate structures.

Structure	Compound	Chemical Shift (ppm)	References
	chondrodite (Mg <sub>5</sub> [SiO <sub>4</sub> ] <sub>2</sub> (OH,F) <sub>2</sub> )	−60	Mägi et al.[31]
	forsterite (Mg <sub>2</sub> SiO <sub>4</sub> )	−61.9	Mägi et al.[31]
	olivine ((Mg,Fe) <sub>2</sub> SiO <sub>4</sub> )	−62	Mägi et al.[31]
	monticellite (CaMgSiO <sub>4</sub> )	−66	Smith et al.[48]
	akermanite (Ca <sub>2</sub> MgSi <sub>2</sub> O <sub>7</sub> )	−73	Smith et al.[48]
	rankinite (Ca <sub>3</sub> Si <sub>2</sub> O <sub>7</sub> )	−74.5	Mägi et al.[31]
	clinoenstatite (MgSiO <sub>3</sub> )	−81; −83	Smith et al.[48]
	orthoestatite (MgSiO <sub>3</sub> )	−82	Mägi et al.[31]
	diopside (CaMgSi <sub>2</sub> O <sub>6</sub> )	−84	Mägi et al.[31]
	fibrous tremolite (Ca <sub>2</sub> Mg <sub>5</sub> [Si <sub>4</sub> O <sub>11</sub> ] <sub>2</sub> (OH) <sub>2</sub> )	−87.8; −92.2	Mägi et al.[31]
	wollastonite (CaSiO <sub>3</sub> )	−89	Hansen et al.[49]
	serpentine (Mg <sub>3</sub> (Si <sub>2</sub> O <sub>5</sub> )(OH) <sub>4</sub> )	−94	Mägi et al.[31]
	talc (Mg <sub>3</sub> (Si <sub>4</sub> O <sub>10</sub> )(OH) <sub>2</sub> )	−98.1	Mägi et al.[31]
	sepiolite (Mg <sub>4</sub> Si <sub>6</sub> O <sub>15</sub> (OH) <sub>2</sub> ·2H <sub>2</sub> O)	−92; −95; −98	Barron et al.[50]
	quartz (SiO <sub>2</sub> )	−108	Smith et al.[48]
	coesite (SiO <sub>2</sub> )	−108.1; 113.9	Smith & Blackwell[51]
	crystalite (SiO <sub>2</sub> )	−108.5	Smith & Blackwell[51]
	tridymite (SiO <sub>2</sub> )	−109.3 - −114	Smith & Blackwell[51]
	silicalite (SiO <sub>2</sub> )	−109.9 - −117	Fyfe et al.[52]
	holdstite (SiO <sub>2</sub> )	−108.9; −115; −119.4	Smith & Blackwell[51]
	silica gel	−91 (Q <sup>2</sup> ); −101 (Q <sup>3</sup> ); −110	Leonardelli et al.[53]
	hydrous α-silica	−92.1 (Q <sup>2</sup> ); −101.6 (Q <sup>3</sup> ); −111.1	Chemtob et al.[54]



**Fig. 3.** Semi-batch dissolution reactor with CO<sub>2</sub> bubbling.

HTS residue-II(b). The strong acid-treated solid residue was denoted as HTS residue-A. The detailed summary of experimental conditions and solid sample notations are given in Table 2.

## 2.2. Determination of dissolution kinetics and identification of silicate structures

During each dissolution experiment, approximately 120  $\mu$ L of slurry samples were taken at a given time interval, and the slurry samples were quickly filtered using a 0.2  $\mu$ m syringe filter and diluted by 2% nitric acid to prevent any precipitation. The samples were analyzed by ICP-OES to determine the Mg and Si concentrations in the liquid phase providing the leaching kinetics of different Mg-silicate materials. At the end of each leaching experiment, the slurry was filtered to collect the solid residue and it was washed with distilled water and ethanol several times. Then, the washed solid residue was dried in a vacuum oven at 70 °C overnight for the subsequent <sup>29</sup>Si solid state MAS NMR and XRPD analyses. To determine crystal structure(s) of each solid residue, the diffraction pattern was collected in the range of 5–70° 2 $\theta$  with a step size of 0.05° and scan time of 0.5 s using the XRPD (X2, Scintag, Inc.).

<sup>29</sup>Si (spin 1/2) MAS NMR measurements were performed using a 3.2 mm Chemagnetics broadband MAS probe, a Varian/Agilent Direct Drive 300 MHz spectrometer operating at a Larmor frequency near 59.9 MHz within a magnetic field of 7.1 T. NMR samples were prepared by packing each solid residue listed in Table 2 into a 3.2 mm zirconia rotor in air at STP. During measurements, compressed dry air was used for both MAS and purge. Free induction nuclear magnetization decays were recorded under a MAS rate of 20 kHz with a single pulse direct polarization sequence (*pulse – acquire – recycle delay*). High power radio frequency pulses of 3.5  $\mu$ s (which is less than the  $\pi/2$  benchmark) were employed for each measurement. Under these conditions, a recycle delay of 5 s was adequate to prevent signal saturation. Depending on the silicate content, typically 30,000 to 50,000 scans were averaged per spectrum. All spectra were referenced to the <sup>29</sup>Si resonance of tetramethylsilane (neat).

Each <sup>29</sup>Si MAS spectrum was analyzed as a composite of weighted component Q<sup>n</sup> lineshapes. The Q<sup>n</sup> MAS lineshapes consist of a central

**Table 2**

Overall experiment condition and name of solid residue.

	Exp#	Acid	Slurry Density (wt %)	Reaction time (min)	In-situ physical and chemical enhancement	Name of solid residues
First leaching	1a	1 atm CO <sub>2</sub> bubbling (carbonic acid, H <sub>2</sub> CO <sub>3</sub> )	0.1	15	–	HTS residue-I(a)
	1b			240	–	HTS residue-I(b)
	1c		5	240	–	HTS residue-I(c) <sup>a</sup>
Secondary leaching	2a		5	240	–	HTS residue-II(a)
	2b				2.25 mm ZB (20 vol%)	HTS residue-II(b) <sup>b</sup>
	2c				2.25 mm ZB (20 vol%), 0.1 M citrate	HTS residue-II(c)
Strong acid leaching	3	2 M HNO <sub>3</sub>	0.5	390	–	HTS residue-A

<sup>a</sup> Starting material of secondary leaching with and without physical and chemical enhancements.<sup>b</sup> Starting material of strong acid leaching.

isotropic resonance (within about  $-60$  ppm to  $-120$  ppm) flanked by spinning sidebands (near  $-400$  ppm and  $+200$  ppm). All peaks were fit by Voigt-type lineshapes [55]. The distribution of different silicate structures/phases was obtained in the usual way through assignment (by identifying the isotropic chemical shift) and integration for each  $Q^n$  unit within the spectrum. Fig. S.1 illustrates the deconvolution procedure for an HTS sample.

### 3. Results and discussion

#### 3.1. Development of different silicate structures during heat-treatment of serpentine

The structural changes of silicate materials (e.g., serpentine) highly depend on the maximum thermal treatment temperature and the heating modes (i.e., prograde heating with a slow ramping rate (e.g.,  $5^\circ\text{C}/\text{min}$ ) or isothermal heating). A thermal decomposition sequence of

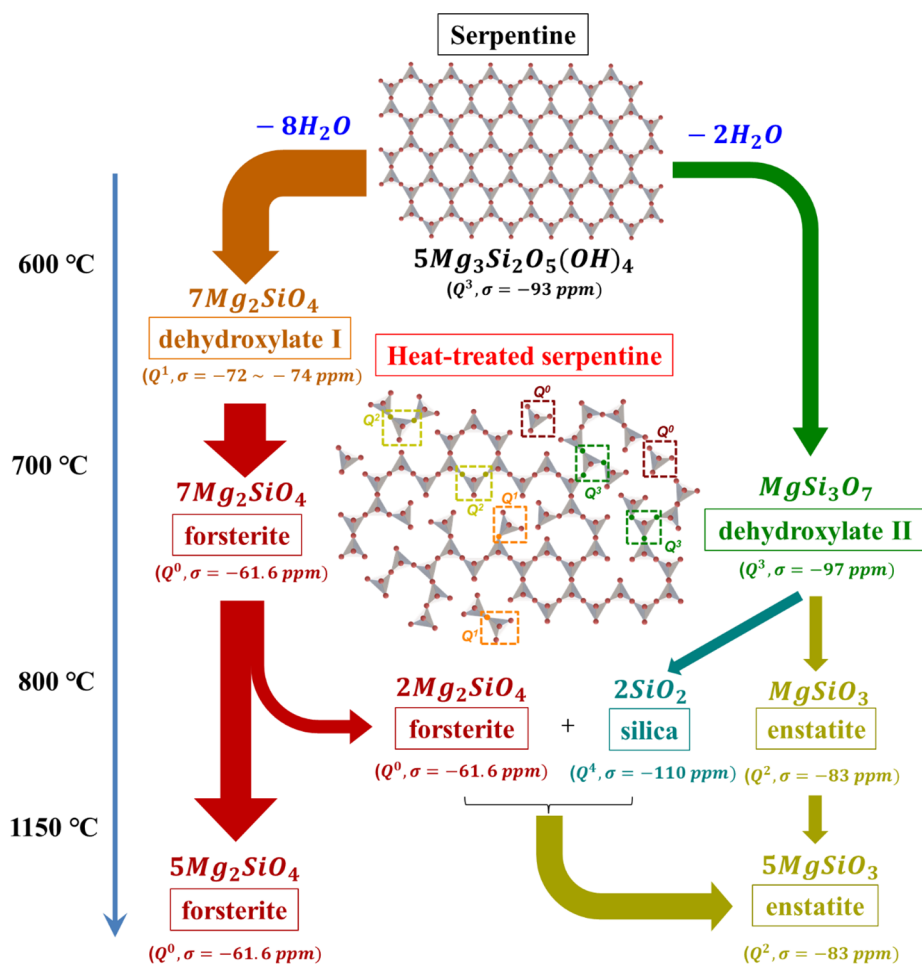


**Fig. 4.** Schematic diagram of thermal decomposition sequence of serpentine with the  $^{29}\text{Si}$  chemical shifts of the various phase, reproduced from Meckenzie and Meinhold [40].



different serpentine polymorphs (i.e., lizardite, chrysotile, antigorite) during prograde heating has been investigated by a number of researchers using X-ray Powder Diffraction (XRPD) and simultaneous Thermalgravimetric and Differential Thermal Analysis (TGA/DTA) [25,27,29,30,32–39]. Generally, the dehydration of serpentine mineral occurs up to 200 °C, and next, the dehydroxylation (the removal of OH groups producing water) proceeds in the range of 600–800 °C. During the dehydroxylation step, the crystal structure of serpentine becomes disrupted and transformed into an amorphous phase. Further heating above 800 °C leads to the formation of crystalline forsterite ( $\text{Mg}_2\text{SiO}_4$ ) and enstatite ( $\text{Mg}_2\text{Si}_2\text{O}_6$ ) from their amorphous phase. The formation of forsterite (< 800 °C) precedes enstatite (> 800 °C) because of lower glass transition temperature ( $T_g$ ) of forsterite than enstatite [30] and

the formation of enstatite seemingly requires a full dehydroxylation of serpentine mineral [26,30,56]. While these studies performed using XRPD were very useful in identifying different silicate phases during the heat treatment of serpentine, this method is limited to crystalline phases and cannot provide insights into amorphous or meta-crystalline phases.

Thus,  $^{29}\text{Si}$  and  $^{25}\text{Mg}$  MAS NMR have been proposed to investigate the amorphous and transient phases. MacKenzie and Meinhold proposed the detailed thermal decomposition sequences of serpentine including the formation of two intermediate phases (dehydroxylate I and II) that would ultimately form forsterite and enstatite crystals (Fig. 4) [40]. Dehydroxylate I is an Mg-rich amorphous phase, characterized by  $\text{Q}^1$  (−73 ppm) structure. This phase is formed at 600–650 °C, and it

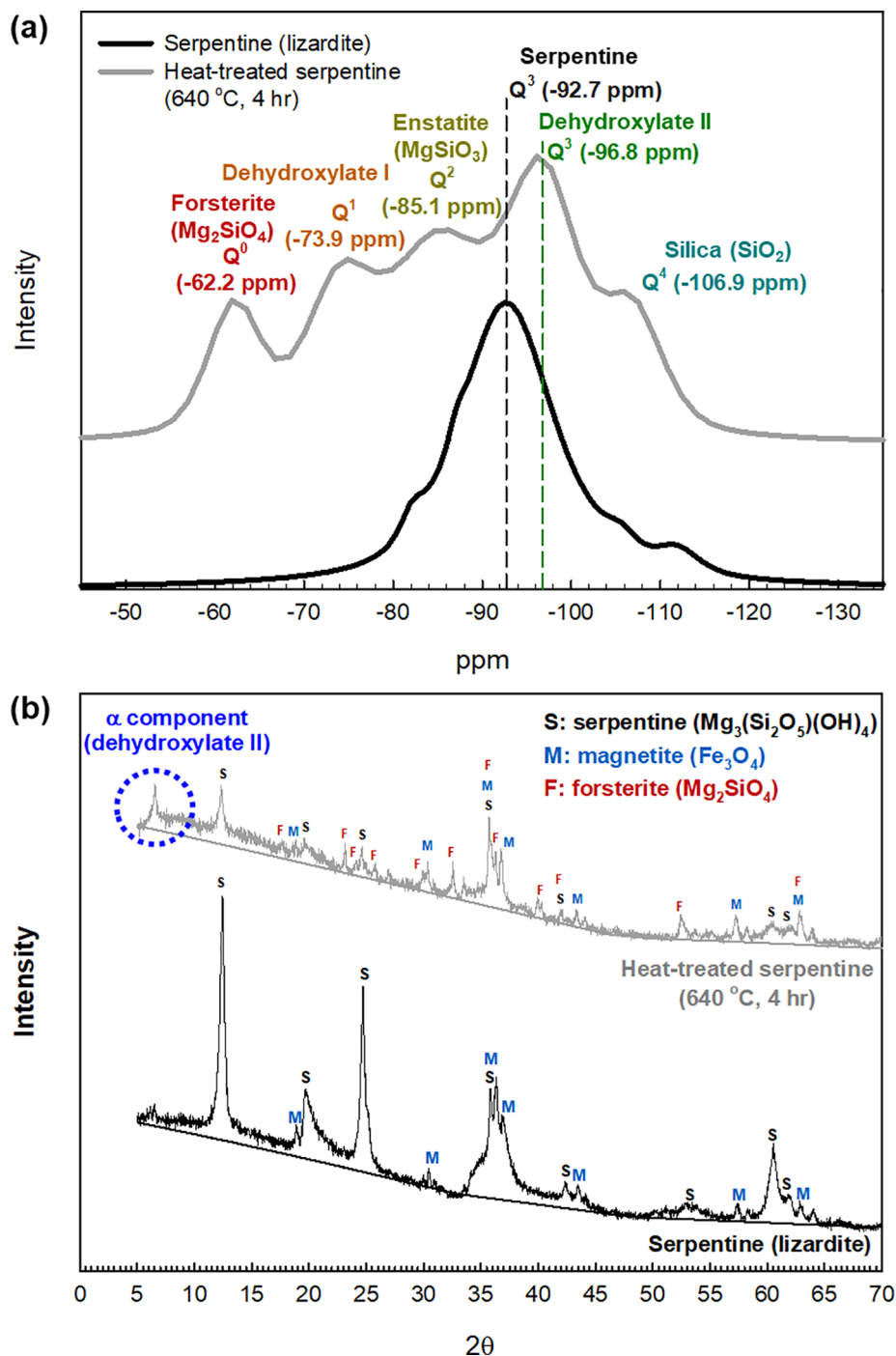


Fig. 5. (a)  $^{29}\text{Si}$  MAS NMR spectra and (b) XRPD patterns of serpentine (lizardite) and heat-treated serpentine which is used in this study.

transforms to forsterite ( $Q^0$ ,  $-61.6$  ppm) at  $670$ – $700$  °C. Simultaneously, at  $670$ – $700$  °C serpentine can also be converted to dehydroxylate II, which is a Si-rich phase having  $Q^3$  ( $-97$  ppm) structure. Dehydroxylate II transforms into a mixture of amorphous enstatite ( $Q^2$ ,  $-83$  ppm) and silica ( $Q^4$ ,  $-110$  ppm) at  $770$ – $800$  °C. Unlike the disordered amorphous dehydroxylate I phase, dehydroxylate II is reported to be more thermally stable and the  $Q^3$  ( $-93$  ppm) Si atoms in this phase are related to the original serpentine 1:1 layered structure with minimal disruption of the parent Si structure and considerable changes in the Mg coordination by heat treatment [40]. Finally, the formation of crystalline enstatite ( $Q^2$ ,  $-83$  ppm) can occur via the reaction between silica ( $Q^4$ ,  $-110$  ppm) and forsterite ( $Q^0$ ,  $-61.6$  ppm) but only at very high temperatures ( $> 1150$  °C) [40,57].

The prograde heating method with a slow temperature ramping successfully identified all the possible thermal decomposition compounds. A series of isothermal heat treatment studies have reported the full dehydroxylation of serpentine at  $575$ – $600$  °C reached after 12 hr in air [58] and at  $647$ – $660$  °C within 1–3 h [41,56,59]. The number of isothermal heating treatment studies performed on serpentine reported the recrystallization of forsterite at  $575$ – $650$  °C, which is significantly lower than the recrystallization temperature identified by the prograde heating method [41,57–59]. Zulumyan et al. [41] described this forsterite phase as “low-temperature forsterite.” They argued that at lower heat treatment temperatures forsterite forms nano-sized crystals and does not grow the crystal size, and thus, these “low-temperature forsterite” were soluble in acid (6–10% HCl) because of nanosized crystals [41].

The heat-treated serpentine (HTS) materials, which were used in this study, were prepared via an isothermal heat treatment at  $640$  °C for

4 hr.  $^{29}\text{Si}$  MAS NMR and XRPD patterns of HTS (gray solid lines) were obtained and compared to those of untreated serpentine (black solid lines). As shown in Fig. 5(a), a single chemical shift peak at  $-92.7$  ppm arising from the sheet-like  $Q^3$  structure was confirmed from the  $^{29}\text{Si}$  MAS NMR spectrum of untreated serpentine [31,40,46]. As serpentine was treated by heat, the formation of two intermediate phases, dehydroxylate I ( $Q^1$ ) and dehydroxylate II ( $Q^3$ ), was observed by the chemical shift peaks at  $-73.9$  ppm and  $-96.8$  ppm, respectively. Other peaks of the HTS NMR spectra at  $-62.2$  ppm,  $-85.1$  ppm, and  $-106.9$  ppm were identified as forsterite ( $\text{Mg}_2\text{SiO}_4$ ,  $Q^0$ ), enstatite ( $\text{MgSiO}_3$ ,  $Q^2$ ), and silica ( $\text{SiO}_2$ ,  $Q^4$ ) [40]. The heat-treated serpentine has more complicated silicate structures consisting of all Q phases ( $Q^0$ – $Q^4$ ) compared to natural serpentine mineral suggesting that its dissolution behaviors would also be complicated.

The XRPD patterns shown in Fig. 5(b) also show the clear differences in crystalline structures of natural and heat-treated serpentine. Natural serpentine mostly contained  $\text{Mg}_3(\text{Si}_2\text{O}_5)(\text{OH})_4$  with a minor quantity of magnetite ( $\text{Fe}_3\text{O}_4$ ). The two most intense peaks were shown at  $2\theta = 12.44^\circ$  and  $24.70^\circ$ , which are associated with the (0 0 1) and (0 0 2) interlamellar reflections [30]. From the heat-treated serpentine sample, dramatically decreased crystalline serpentine peaks and the appearance of forsterite were observed, indicating that most of the crystalline serpentine structure was disrupted and the thermal decomposition was accompanied by the simultaneous re-crystallization of the forsterite phase. As discussed earlier, this re-crystallized Mg-silicate phase would be the nanocrystals of “low-temperature forsterite,” which can be easily dissolved in acids [41]. The evidence of the formation of intermediate phases was also found at  $2\theta = 6$ – $7.5^\circ$  in the XRPD pattern of HTS [25,30,58]. The appearance of the low angle feature ( $d$  spacing

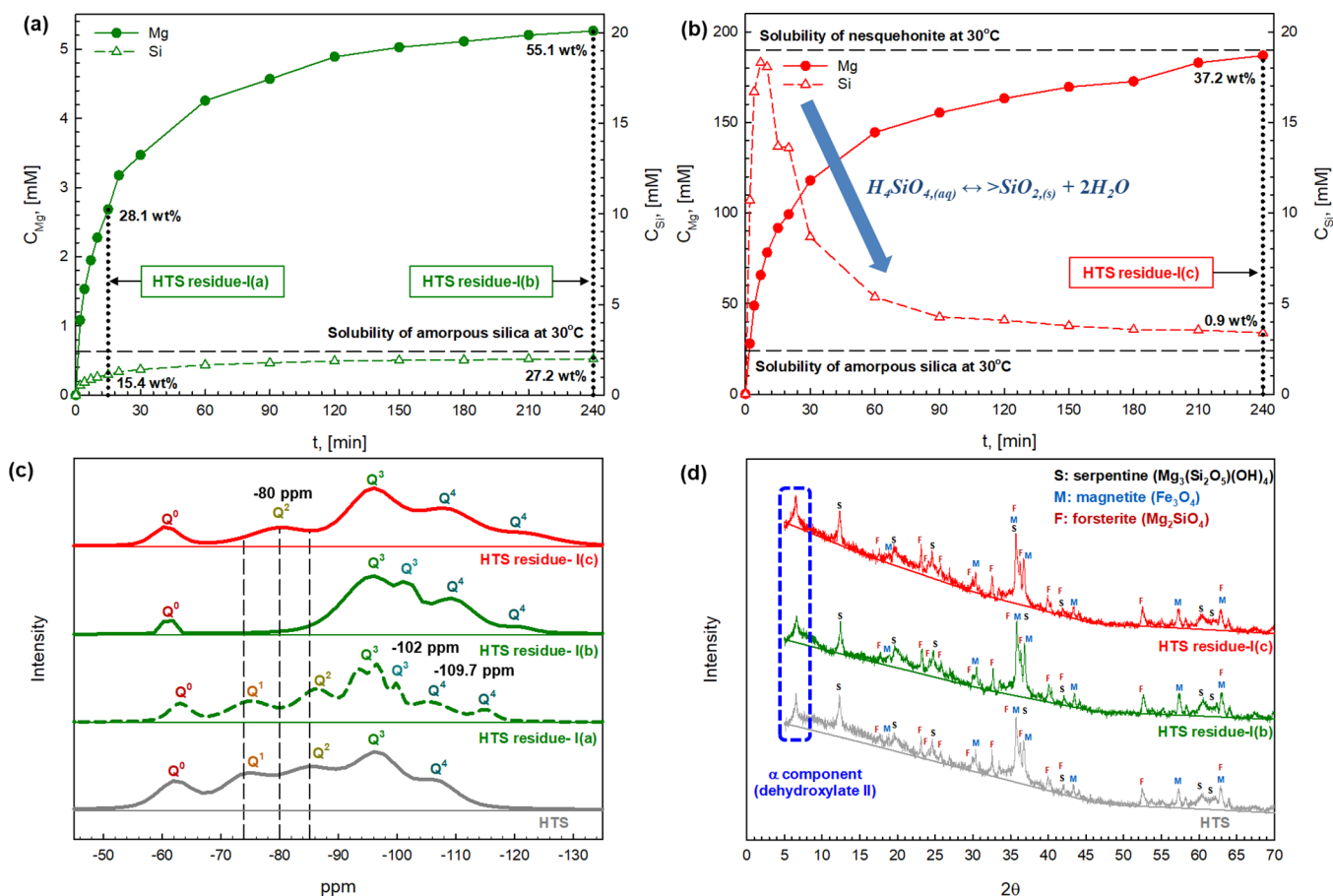


**Fig. 6.** First leaching of heat-treated serpentine at 30 °C and 1 atm CO<sub>2</sub>. Mg and Si concentration profile of (a) far-from-equilibrium condition (0.1 wt% slurry density, Ex#: 1a, 1b) and (b) near-equilibrium condition (5 wt% slurry density, Ex#: 1c) during the first leaching. (c)  $^{29}\text{Si}$  MAS NMR spectra and (b) XRPD patterns of heat-treated serpentine (HTS) residue-I.

of 14.7 Å) was likely caused by the formation of a meta-serpentine phase ( $\alpha$  component), corresponding to a doubling of the 7.34 Å interlamellar spacing at (0 0 1) [30]. A previous study suggested that this “ $\alpha$  component” may correspond to  $Q^3$  meta lizardite structure (dehydroxylate II), which is formed by tearing the original  $Q^3$  structure (lizardite) during the heat treatment process [29]. Thus, the broad chemical shift peak centered at  $-96.8$  ppm ( $Q^3$ ) in the NMR spectra of HTS (Fig. 5(a)) would be attributed to mostly the dehydroxylate II phase with a minor quantity of original crystalline serpentine structure. Although the formations of  $Q^1$  (dehydroxylate I) and  $Q^2$  (enstatite,  $MgSiO_3$ ) were confirmed in the  $^{29}Si$  NMR spectrum (Fig. 5(a)), characteristic diffraction peaks of dehydroxylate I and enstatite were not identified in the XRPD pattern of heat-treated serpentine shown in Fig. 5(b), confirming that  $Q^1$  and  $Q^2$  structures in HTS were amorphous phases.

### 3.2. Elemental (Mg and Si) leaching behaviors and silicate structural alterations of heat-treated serpentine (HTS) in carbonic acid

In order to establish a relationship between elemental (particularly, Mg and Si) extraction behaviors and HTS silicate structures ( $Q^0$ – $Q^4$ ) changes in carbonic acid, the Mg and Si concentration profiles were obtained and the results were compared with the findings from  $^{29}Si$  NMR and XRPD spectrum of the solid residue samples, which were collected after the leaching experiments (experimental conditions summarized in Table 2).

Experiments were performed under both far-from-equilibrium (0.1 wt% of SD) and near-equilibrium (5 wt% of SD) conditions. The Mg and Si concentration profiles measured during the “First leaching” step (the dissolution of fresh HTS) are shown in Fig. 6(a) and (b) with solubility limits of nesquehonite ( $MgCO_3 \cdot 3H_2O$ ) and amorphous silica ( $SiO_2$ ) indicated [16]. The fresh HTS exhibited a rapid initial Mg extraction kinetic indicating that the surface dissolution reaction was the dominant mechanism and 28.1 wt% of Mg was extracted within 15 min. At 15 min, the Mg to Si concentration ratio ( $C_{Mg}/C_{Si} = 2.4$ ) was higher than the elemental ratio in fresh HTS ( $n_{Mg}/n_{Si} = 1.3$ ) indicating an incongruent dissolution behavior of fresh HTS, which is strong evidence of the formation of a Si-rich passivation layer on the surface of mineral particles [60]. Subsequently, a reduced Mg extraction kinetic was observed due to the mass transfer limitation and it took 225 min to extract an additional 27.0 wt% of Mg reaching the total Mg extraction of 55.1 wt%. Thus, the structures and chemical stability of the silicate phase remaining in the Si-rich passivation layer would be important factors to the overall extraction of Mg and other metals from minerals.

The solid residue samples collected after 15 and 240 min of the first leaching process were denoted as HTS residue-I(a) and (b), respectively, and their  $^{29}Si$  NMR spectra are shown in Fig. 6(c). In the  $^{29}Si$  NMR spectrum of HTS residue-I(a), decreases in the intensity of  $Q^0$ ,  $Q^1$ , and  $Q^2$  peaks were found indicating the dissolution of forsterite, dehydroxylate I and enstatite phases in the weak acidic solution (i.e., carbonic acid produced by bubbling  $CO_2$ ). At the same time, a chemical shift at  $-102$  ppm was observed and assigned to the  $Q^3$  ( $(SiO)_3SiOH$ ) structure, which was formed by the ion-exchange reaction ( $Mg^{2+} \leftrightarrow 2H^+$ ) on the HTS surface. These Si atoms bearing OH groups can be condensed/polymerized resulting in the formation of amorphous silica layer ( $(SiO)_4Si$ ) [60–62], which resulted in the chemical shifts at  $-106$  ppm and  $-115$  ppm identified as the three-dimensional cross-linked  $Q^4$  structure. Thus, these  $Q^3$  and  $Q^4$  structures are evidence of the formation of the Si-rich passivation layer during HTS dissolution [46,47,63].

As the dissolution of HTS in carbonic acid continued beyond 15 min, the chemical shifts at  $-73.9$  ppm and  $-85.1$  ppm disappeared in the HTS residue-I(b) suggesting complete digestion of  $Q^1$  (dehydroxylate I) and  $Q^2$  (enstatite) phases after 240 min dissolution reaction (Fig. 6(c)). In contrast, the chemical shifts for  $Q^0$  (forsterite,  $-61.1$  ppm) and  $Q^3$  (dehydroxylate II and serpentine,  $-95.7$  ppm) structures were still

observed and the crystalline phase of  $\alpha$  component, serpentine, and forsterite remained the same according to the XRPD pattern of HTS residue-I(b) (Fig. 6(d)). Thus, it was concluded that the amorphous  $Q^1$  (dehydroxylate I) and  $Q^2$  (enstatite) structures are more soluble than crystalline  $Q^0$  (forsterite) and  $Q^3$  (dehydroxylate II and serpentine) structures. Tuning these silicate structures would be important during the heat treatment of silicate materials including serpentine in order to optimize their dissolution behaviors.

Fig. 6(b) shows the Mg and Si concentration profiles of the “First leaching” step when it was performed under near-equilibrium condition (5 wt% of SD). In contrast to 0.1 wt% SD case (Fig. 6(a)), a solution with a high Mg concentration close to the solubility limit of nesquehonite ( $MgCO_3 \cdot 3H_2O$ ) was achieved. Unlike the previous far-from-equilibrium case, the concentration of Si ( $C_{Si}$ ) was rapidly supersaturated at the beginning of the HTS dissolution and dissolved Si was quickly re-precipitated onto the HTS surface as a new amorphous silica phase ( $H_4SiO_4(aq) \leftrightarrow SiO_{2(s)} + 2H_2O$ ) forming the Si-rich passivation layer as evidenced in the broader  $^{29}Si$  NMR  $Q^4$  peaks. The  $C_{Mg}/C_{Si}$  ratio at 240 min was found to be 55.3, which was much higher than the ratio observed under the far-from-equilibrium condition ( $C_{Mg}/C_{Si} = 2.6$  at 240 min) leading to the development of the Si-rich passivation layer [14,16,64,65]. The near-equilibrium condition (Fig. 6(b)) also showed a rapid initial Mg extraction, followed by a reduced extraction kinetics with mass transfer limitation when the reprecipitation of extracted Si began. The final extent of Mg extraction (37.2 wt%) was lower than that of the far-from-equilibrium case (55.1 wt%).

The fate of different silicate phases is shown in Fig. 6(c) of  $^{29}Si$  NMR spectrum of HTS residue-I(c) (the solid residue collected after the near-equilibrium HTS dissolution experiment). These NMR chemical shifts provide additional evidence of the significant formation of the Si-rich passivation layer. The chemical shift peaks for  $Q^4$  ( $SiO_2$ ) were more intense and broader than those from HTS residue-(a) and HTS residue-(b) (far-from-equilibrium cases). The existence and shifting of the  $Q^2$  peak at  $-80$  ppm (amorphous enstatite) [66] and the more intense  $Q^0$  peak elucidate the limited dissolution of forsterite ( $Q^0$ ) and altered the structure of enstatite ( $Q^2$ ) in the presence of the Si-rich passivation layer.

### 3.3. Effects of in-situ grinding and chemical ligand on the dissolution behaviors of different silicate phases and their chemical changes

As discussed in the previous section, the “First leaching” step of HTS resulted in the development of different and new silicate structures on the HTS surface. Thus, in order to investigate the dissolution behaviors of these different silicate structures, the “Secondary leaching” study was conducted with the HTS residue-I(c) with a fully developed Si-rich passivation layer (collected after the “First leaching” experiment). The  $C_{Mg}$  and  $C_{Si}$  profiles of the “secondary leaching” experiments are shown in Fig. 7(a). As expected from the data shown in Fig. 6(b), Mg and Si dissolution kinetics were very slow and only an additional 5.3 wt% of Mg was extracted from the HTS residue-I(c) after 240 min of secondary leaching because of the fully developed Si-passivation layer.

First, an internal grinding experiment was performed by incorporating the grinding media (2.25 mm zirconia beads) into the slurry reactor to reduce/remove the passivation layer and potentially disorder the crystal structures of HTS particles [67,68]. After 4 hr dissolution with the grinding media, the extent of additional Mg extraction (16.5 wt%) was three times higher than that of the base case without any activation method (5.3 wt%). When a Mg-targeting ligand (0.1 M of Na-citrate) was added to the system, the combined chemical and physical activations of HTS residue resulted in a further enhancement reaching a total of 17.8 wt% of additional Mg leaching. While these data were promising, it was important to investigate how chemical and physical activations would influence the silicate phases within the HTS residue.

The solid residue samples collected after the “Secondary leaching”



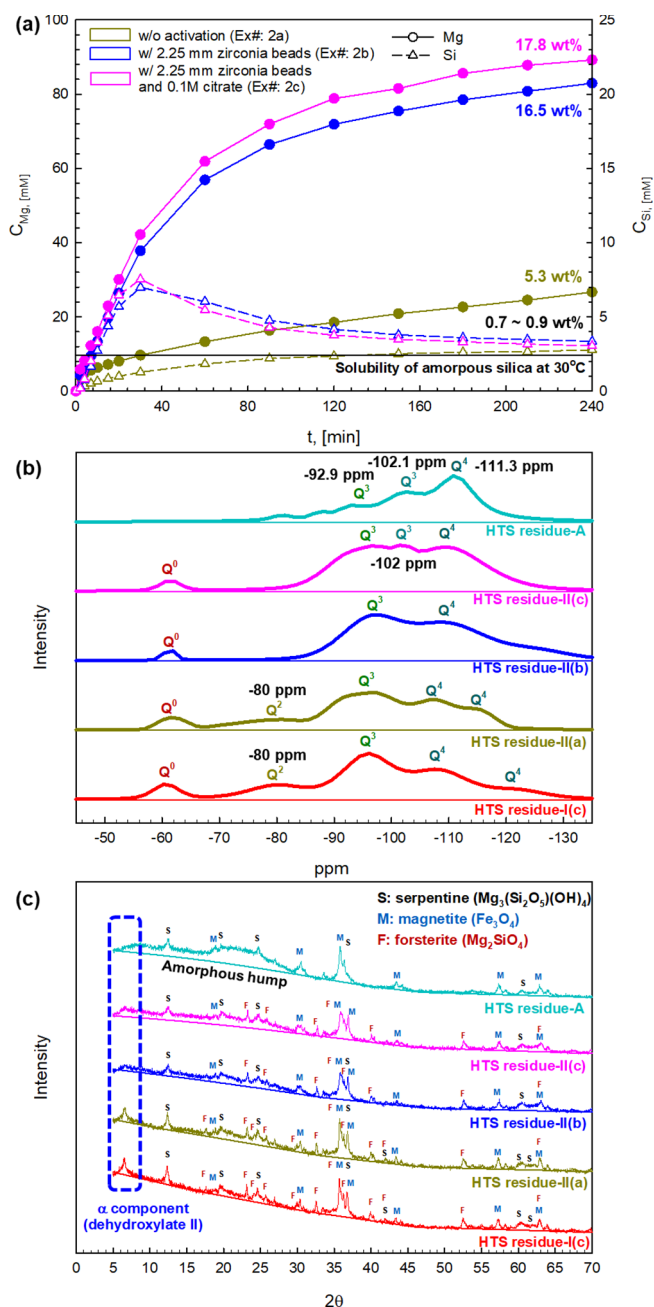


**Fig. 7.** Secondary and acid leaching of heat-treated serpentine. (a) Mg and Si concentration profile during the secondary leaching (5 wt% slurry density, 30 °C). (b) <sup>29</sup>Si MAS NMR spectra and (c) XRPD patterns of heat-treated serpentine residue-II and residue-A.

step were denoted as HTS residue-II(a) (without activation), HTS residue-II(b) (with grinding media) and HTS residue-II(c) (with grinding media and 0.1 M citrate). Their <sup>29</sup>Si NMR spectra and XRPD patterns are shown in Fig. 7(b) and (c). Because of the limited Mg extraction resulted from the passivation effect, the chemical shift at -80 ppm was still identified in the HTS residue-II(a) sample indicating an incomplete dissolution of Q<sup>2</sup> (amorphous enstatite) structure. At the same time, changes in crystalline Q<sup>0</sup> (forsterite) and Q<sup>3</sup> (dehydroxylate II and serpentine) peaks were not noticed from the NMR and XRPD spectrum of HTS residue-II(a) indicating that the additional 5.3 wt% of Mg extraction was mostly from the slow dissolution of amorphous Q<sup>2</sup> (enstatite) structure.

On the other hand, the *in-situ* grinding yielded a significant improvement in Mg/Si extraction from HTS residue-I(c) (Fig. 7(a)). Our

previous studies have shown that by mechanically removing the fully developed Si-rich passivation layer on the mineral surface, leaching of metals from silicate structures can be significantly enhanced [69,70]. The <sup>29</sup>Si NMR spectra of HTS residue-II(b) in Fig. 7(b) confirmed the complete digestion of amorphous Q<sup>2</sup> structure (-80 ppm, enstatite) and the decreased peak intensity of crystalline Q<sup>0</sup> (forsterite) structure. As the surface of HTS particles was refreshed, these more soluble Mg-silicate phases were first dissolved and the data support that behavior. According to the XRPD patterns of the HTS residue-II(b) shown in Fig. 7(c), the decrease in α component (dehydroxylate II, 2θ = 6–7.5°) and serpentine reflections also evidence the dissolution of the crystalline phases. This XRPD data agrees with the previously reported phenomena of disrupting the crystal structures of natural minerals via particle grinding [71–74]. Thus, the additional 16.5 wt% of Mg extraction in the presence of *in-situ* grinding would be attributed to the dissolution of both amorphous (Q<sup>2</sup>: enstatite) and crystalline (Q<sup>0</sup>: forsterite, Q<sup>3</sup>: dehydroxylate II and serpentine) structures. Even with the *in-situ* grinding, 46.3 wt% of Mg (out of the total initial mass of Mg in HTS) remained in the HTS residue-II(b) because the solvent (low-cost carbonic acid) was not strong enough.

As 0.1 M of citrate solution was added to the *in-situ* grinding system, the extent of additional Mg extraction was slightly improved from 16.5 wt% to 17.8 wt% after 4 hr extraction as shown in Fig. 7(a). Under the given mild pH (6–7) and temperature (30 °C) conditions, the organic ligand (citrate) was expected to chemically improve the ion exchange reaction,  $Mg^{2+} \leftrightarrow 2H^{+}$ , on the HTS residue surface by forming a complex with Mg. The <sup>29</sup>Si NMR spectra of HTS residue-II(c) in Fig. 7(b) shows the formation of the new Q<sup>3</sup> ((SiO)<sub>3</sub>SiOH) structure (-102 ppm) on the particle surface, which was different from simple ion exchange reaction by the proton from the carbonic acid. Since Q<sup>3</sup> is an amorphous phase, the XRPD spectra of the HTS residue-II(c) (Fig. 7(c)) did not show significant evidence on the effect of ligand on the mineral dissolution.

While the dissolution behaviors of different silicate structures (Q<sup>0</sup>–Q<sup>4</sup>) were interesting, tuning their structures alone would not achieve the complete extraction of Mg from HTS. Thus, in order to extract the remaining 46.3 wt% of Mg in the HTS residue-II(b) and to further evaluate the stability and the solubility of Q<sup>3</sup> (dehydroxylate II and serpentine) and Q<sup>0</sup> (forsterite) phases, a strong 2 M HNO<sub>3</sub> acidic solvent was used to dissolve the HTS residue-II(b) sample. The solid residue collected after this “Strong acid leaching” step was denoted HTS residue-A and its <sup>29</sup>Si NMR spectra and XRPD patterns are shown in Fig. 7(b) and (c), respectively. The crystalline forsterite and α component (dehydroxylate II) were completely digested and the HTS residue-A was enriched with amorphous silica with a minor quantity of undissolved crystalline serpentine phase after the extensive Mg leaching by the strong acid. The chemical shift at -92.9 ppm corresponds to the undissolved crystalline serpentine Q<sup>3</sup> structure [46] and the intense chemical shift peaks at -102.1 ppm and -111.3 ppm are attributed to Q<sup>3</sup> ((SiO)<sub>3</sub>SiOH) and Q<sup>4</sup> ((SiO)<sub>4</sub>Si) hydrous amorphous silica phases [53,54]. The broad peak between 15° and 30° 2θ in the XRPD pattern is additional evidence of the formation of the amorphous silica as most of the Mg leached out of heat-treated serpentine [75].

### 3.4. Leaching mechanisms and sequences of heat-treated serpentine mapped based on silicate structures identified by <sup>29</sup>Si solid state MAS NMR

Based on the solution chemistry and quantitative NMR analysis, the solubility of each silicate structure (Q<sup>0</sup>–Q<sup>4</sup>) was evaluated and the overall dissolution mechanisms of heat-treated serpentine is proposed in Fig. 8(c) to provide insights into the chemical stability and leaching behaviors of various silicate materials. The relative concentrations of Q<sup>n</sup> phases were determined via the deconvolution of <sup>29</sup>Si MAS NMR spectra as explained in the experimental section.

As shown in Fig. 8(b), the fresh HTS was a mixture of Q<sup>0</sup> (11.4%), Q<sup>1</sup> (15.3%), Q<sup>2</sup> (32.3%), Q<sup>3</sup> (26.9%), and Q<sup>4</sup> (14.1%) structures. During

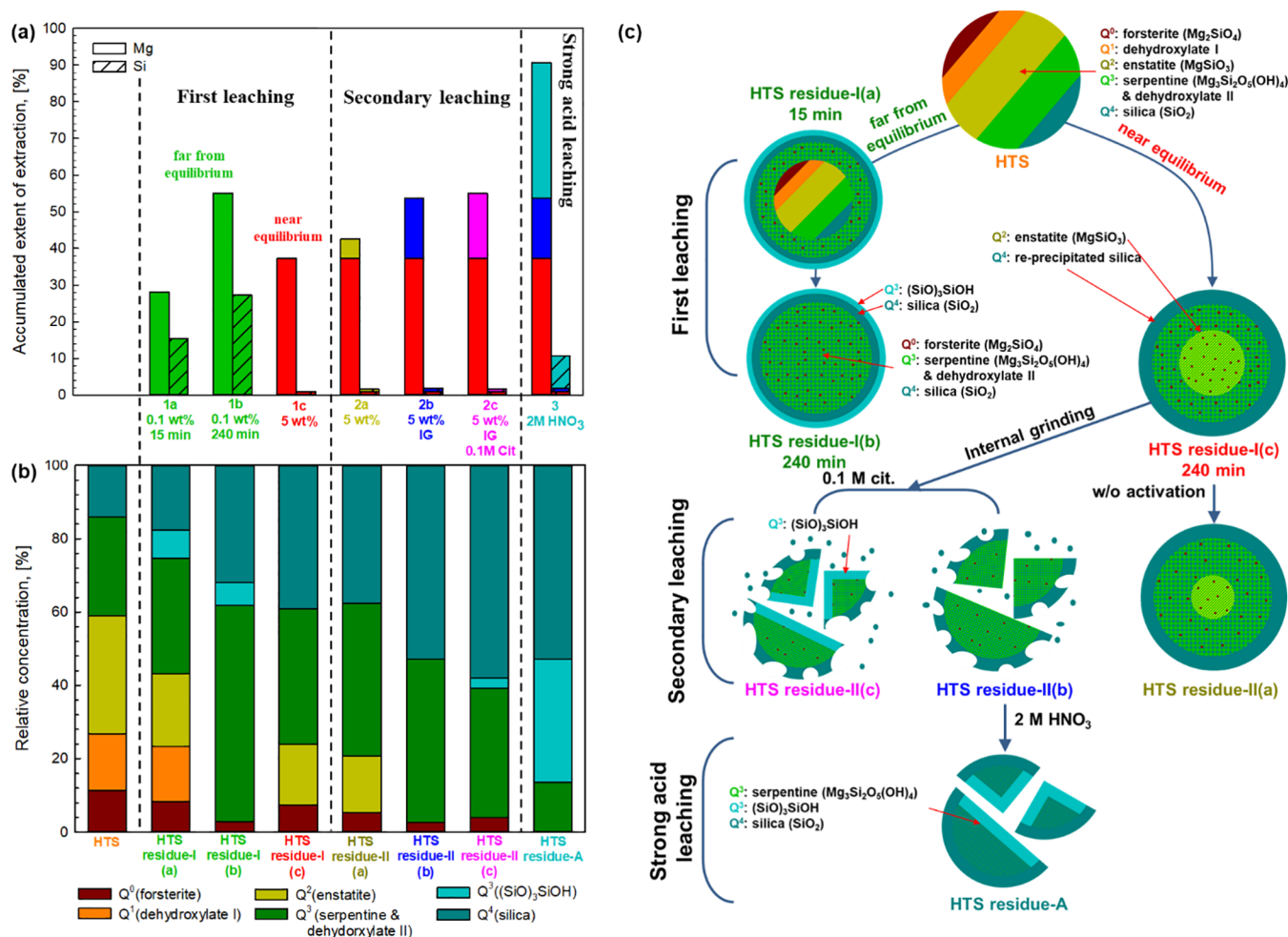


**Fig. 8.** (a) Accumulated extent of Mg and Si extraction of first, secondary, and strong acid leaching. (b) Relative concentration of various Si phase (Q<sup>0</sup> - Q<sup>4</sup>) in HTS residue. (c) Schematic diagram of heat-treated serpentine silicate structure change in the acid leaching process.

the “First leaching” step, the HTS underwent two different dissolution pathways depending on the slurry density condition (i.e., far-from-equilibrium (0.1 wt%) or near-equilibrium (5.0 wt%)). After 15 min dissolution of the far-from-equilibrium condition (Exp# in Table 2: 1a), more Mg (28.1 wt% of the initial Mg) was extracted compared to Si (15.4 wt% of the initial Si) and the new Q<sup>3</sup> phase ((SiO<sub>2</sub>)<sub>3</sub>SiOH) appeared and the amount of Q<sup>4</sup> phase (SiO<sub>2</sub>, silica) was increased. This confirmed the formation of the Si-rich passivation layer resulted from the incongruent dissolution between Mg and Si as previously discussed based on Fig. 6(a). Thus, the HTS residue-I(a) would have a core-shell structure with the core consisting of the same silicate composition as the fresh HTS and the shell composed of Si-rich phase (Fig. 8(c) – the dissolution path on the left). As the dissolution reaction continued for an additional 225 min (total 240 min), the HTS reached 55.1 wt% and 27.2 wt% of Mg and Si extractions, respectively (Exp# in Table 2: 1b). The HTS residue particle would be relatively homogenous with the outer shell containing the new Q<sup>3</sup> structure (light blue in Fig. 8(c)) since the Q<sup>1</sup> (dehydroxylate I, orange in Fig. 8) and Q<sup>2</sup> (enstatite, dark yellow in Fig. 8) structures were completely dissolved after 240 min as shown in the NMR analysis of HTS residue-I(b).

As discussed earlier with Fig. 6(b), in the near-equilibrium dissolution pathway, significant Si was leached out and they were reprecipitated as amorphous silica on the HTS surface because of the solubility limitation of SiO<sub>2</sub>. Because of the significant Si reprecipitation, a large amount of Q<sup>4</sup> structure (SiO<sub>2</sub>, blue green in Fig. 8) was observed instead of the Q<sup>3</sup> structure ((SiO<sub>2</sub>)<sub>3</sub>SiOH, light blue in Fig. 8) in

the NMR analysis of HTS residue-I(c). The undissolved Q<sup>2</sup> (enstatite) structure was still observed in the NMR analysis of HTS residue-I(c) suggesting a Q<sup>2</sup> (enstatite) rich core structure with a fully developed Si-rich passivation layer as shown in Fig. 8(c) (the dissolution path on the right). Based on the quantitative NMR analyses of the “First leaching” step solid residue samples shown in Fig. 8(b), the solubilities of each silicate structure were compared and they are in the order of Q<sup>1</sup> (dehydroxylate I) > Q<sup>2</sup> (enstatite) >> Q<sup>0</sup> (forsterite) > Q<sup>3</sup> (dehydroxylate II and serpentine).

After the “Secondary leaching” step without any activation method (Exp# in Table 2: 2a), only 5.3 wt% of Mg was extracted from the HTS residue-I(c) and the overall structure of HTS solid residue particle would not have significantly changed (Fig. 8(c) – HTS residue-II(a) in the second row on the right). The quantitative NMR analysis of HTS residue-II(a) indicated that only small amounts of Q<sup>0</sup> (forsterite) and Q<sup>2</sup> (enstatite) structures were dissolved slightly, reducing the size of the unreacted core of the mineral particle.

The *in-situ* grinding in the “Secondary leaching” step, both with and without the chemical ligand (citrate), significantly improved the extent of Mg extraction by physically removing the passivation layer and reducing particle sizes (and also disordering the crystalline  $\alpha$  component (dehydroxylate II) and original serpentine phase) as illustrated in Fig. 8(c) – HTS residue-II(c) and HTS residue-II(b) in the second row. As a result, 53.7 wt% and 55.0 wt% of the total extent of Mg extraction (Exp# in Table 2: 2b and Exp# in Table 2: 2c) were achieved, which was comparable to the far-from-equilibrium condition (55.1 wt%) in

“First leaching” step (Exp# in Table 2: 1b) (Fig. 8(a)). With the increased surface area and exposed inner unreacted core surfaces, the  $Q^2$  (enstatite) in the core of the HTS residue-I(c) was completely digested and the particles became more homogenous with the residual  $Q^4$  Si-rich passivation layer (silica, blue green) and the newly formed  $Q^3$  ((SiO)<sub>3</sub>SiOH, light blue) structure.

The final “Strong acid leaching” case shown in Fig. 8(c) – bottom figure – illustrates the complete extraction of Mg from the crystalline  $Q^0$  (forsterite) and  $Q^3$  (dehydroxylate II or  $\alpha$  component) structures although the crystalline  $Q^3$  serpentine phase (green) still remained in the HTS residue-A. Thus, the total extent of Mg extraction after the consecutive First, Secondary and Strong acid leaching processes was not 100 wt% but 90.6 wt% as shown in Fig. 8(a) indicating that 9.4 wt% of Mg in HTS residue-A was in the form of crystalline serpentine phase ( $Q^3$ ), which is very stable and insoluble. The quantitative NMR analysis in Fig. 8(b) indicated that the HTS residue-A is enriched with hydrous amorphous silica,  $Q^3$  ((SiO)<sub>3</sub>SiOH) and  $Q^4$  ((SiO)<sub>4</sub>Si), with 13.6% of crystalline serpentine phase ( $Q^3$ ). Therefore, the solubilities of each crystalline silicate structure would be in the order of  $Q^0$  (forsterite) >  $Q^3$  (dehydroxylate II) >  $Q^3$  (serpentine).

#### 4. Conclusions

In this study, the chemical and structural changes occurring within the Mg-silicate materials during the heat treatment and subsequent dissolutions in the presence of CO<sub>2</sub> (i.e., carbonic acid) were investigated with <sup>29</sup>Si MAS NMR, XRPD, and ICP-OES. The use of the <sup>29</sup>Si MAS NMR technique allowed the in-depth investigation of amorphous phases, which were found to play important roles in the dissolution behaviors of silicate materials. After the heat treatment of serpentine (hydrous Mg-silicate material), the formations of amorphous ( $Q^1$ : dehydroxylate I,  $Q^2$ : enstatite,  $Q^4$ : silica) and crystalline ( $Q^0$ : forsterite,  $Q^3$ : dehydroxylate II and serpentine) phases were confirmed. The incongruent Mg and Si dissolution behavior and reprecipitation of extracted Si eventually resulted in the formation of the Si-rich passivation layer on the mineral particles,  $Q^3$  ((SiO)<sub>3</sub>SiOH) and  $Q^4$  ((SiO)<sub>4</sub>Si). The elemental extraction of Mg from HTS was limited if there is a significant development of  $Q^3$  ((SiO)<sub>3</sub>SiOH) and  $Q^4$  ((SiO)<sub>4</sub>Si) layers. In-situ grinding of HTS particles enhanced the overall Mg leaching via two mechanisms: the physical removal of the Si-rich passivation layer exposing more soluble silicate structure ( $Q^2$ ) in the inner unreactive core and the distortion of crystalline  $\alpha$  component ( $Q^3$ ). By combining chemical and physical activation approaches, a total 55.0 wt% of Mg was extracted from HTS. This value was increased to 90.6 wt% when a strong acid (e.g., 2 M HNO<sub>3</sub>) was used as the solvent. The most stable Mg-silicate structures were the crystalline  $Q^0$  (forsterite) and  $Q^3$  (dehydroxylate II and serpentine). The solubilities of silicate structures were qualitatively evaluated based on the NMR and XRPD analyses and they are in the order of  $Q^1$  (dehydroxylate I) >  $Q^2$  (enstatite) >  $Q^0$  (forsterite) >  $Q^3$  (dehydroxylate II) >  $Q^3$  (serpentine) (>  $Q^4$  (silica)). Therefore, the heat treatment condition for serpentine should be optimized to maximize the formations of the amorphous  $Q^1$  (dehydroxylate I) and  $Q^2$  (enstatite) structures if the maximum Mg extraction is targeted for the carbon mineralization technology that fixes CO<sub>2</sub> into solid carbonates. On the other hand, if Si-bearing materials will be used for other energy and environmental applications (e.g., as a substrate for CO<sub>2</sub> capture materials), more stable silicate structures such as  $Q^3$  and silica ( $Q^4$ ) may be preferred.

#### Declaration of Competing Interest

The authors declare that they have no known competing financial interests or personal relationships that could have appeared to influence the work reported in this paper.

#### Acknowledgments

This study was supported by Mineral Carbonation International (MCI) in Australia (discussions on leaching behaviors of silicate materials for carbon sequestration) and the Breakthrough Electrolytes for Energy Storage (BEES), an Energy Frontier Research Center funded by the U.S. Department of Energy (DOE), Office of Science, Basic Energy Sciences (BES), under Award DE-SC0019409 (development of Si-29 NMR method to study silicate materials). The authors, Guanhe Rim and Ah-Hyung Alissa Park (BEES member), contributed the discussions on the leaching behaviors of silicate materials based on the NMR data, while Ariane K. Marchese, Phillip Stallworth and Steven G. Greenbaum (BEES member) developed the Si-29 NMR method that provided the structural identification of silicate materials. AKM acknowledges support from the U.S. National Institutes of Health RISE Program (GM 060665).

#### Appendix A. Supplementary data

Supplementary data to this article can be found online at <https://doi.org/10.1016/j.cej.2020.125204>.

#### References

- [1] N.O.A.A. Research, Recent Global CO<sub>2</sub> Trend, < [https://www.esrl.noaa.gov/gmd/ccgg/trends/gl\\_trend.html](https://www.esrl.noaa.gov/gmd/ccgg/trends/gl_trend.html) > (2019).
- [2] M. Scheffer, V. Brovkin, P.M. Cox, Positive feedback between global warming and atmospheric CO<sub>2</sub> concentration inferred from past climate change, *Geophys. Res. Lett.* 33 (2006).
- [3] Special Report, Global Warming of 1.5 °C, Intergovernmental Panel on Climate Change (2018).
- [4] P. Falkowski, R.J. Scholes, E. Boyle, J. Canadell, D. Canfield, J. Elser, N. Gruber, K. Hibbard, P. Hogberg, S. Linder, F.T. Mackenzie, B. Moore, T. Pedersen, Y. Rosenthal, S. Seitzinger, V. Smetacek, W. Steffen, The global carbon cycle: A test of our knowledge of earth as a system, *Science* 290 (2000) 291–296.
- [5] Report of the Mission Innovation Carbon Capture, Utilization, and Storage Expert's Workshop, MISSION INNOVATION Accelerating the Clean Energy Revolution, Saudi Aramco, Saudi Arabia; Department of Energy, United States, 2017, pp. 26–28.
- [6] E. National Academies of Sciences, and Medicine, Gaseous Carbon Waste Streams Utilization: Status and Research Needs, Washington, DC: The National Academies Press (2019).
- [7] W.A. Deer, R.A. Howie, J. Zussman, An Introduction To The Rock-Forming Minerals, 2nd ed., Longman Scientific & Technical; Wiley, New York, NY, 1992.
- [8] W. Seifritz, CO<sub>2</sub> disposal by means of silicates, *Nature* 345 (1990) 486.
- [9] A. Sanna, M. Uibu, G. Caramanna, R. Kuusik, M.M. Maroto-Valer, A review of mineral carbonation technologies to sequester CO<sub>2</sub>, *Chem. Soc. Rev.* 43 (2014) 8049–8080.
- [10] F.L. Goff, Carbon dioxide sequestering using ultramafic rocks, *Environ. Geosci.* 5 (1998) 89–101.
- [11] E. National Academies of Sciences, and Medicine, “3 Mineral Carbonation to Produce Construction Materials.” Gaseous Carbon Waste Streams Utilization: Status and Research Needs, DC: The National Academies Press (2019).
- [12] T.G.C.I. CO<sub>2</sub> Sciences, Global Roadmap for Implementing CO<sub>2</sub> Utilization, (2016).
- [13] A.A. Olajire, A review of mineral carbonation technology in sequestration of CO<sub>2</sub>, *J. Petrol. Sci. Eng.* 109 (2013) 364–392.
- [14] F. Farhang, M. Rayson, G. Brent, T. Hodgins, M. Stockenhuber, E. Kennedy, Insights into the dissolution kinetics of thermally activated serpentine for CO<sub>2</sub> sequestration, *Chem. Eng. J.* 330 (2017) 1174–1186.
- [15] L.C. Pasquier, G. Mercier, J.F. Blais, E. Cecchi, S. Kentish, Reaction mechanism for the aqueous-phase mineral carbonation of heat-activated serpentine at low temperatures and pressures in flue gas conditions, *Environ. Sci. Technol.* 48 (2014) 5163–5170.
- [16] M. Werner, S. Hariharan, M. Mazzotti, Flue gas CO<sub>2</sub> mineralization using thermally activated serpentine: from single- to double-step carbonation, *PCCP* 16 (2014) 24978–24993.
- [17] S. Hariharan, M. Repmann-Werner, M. Mazzotti, Dissolution of dehydroxylated lizardite at flue gas conditions: III. Near-equilibrium kinetics, *Chem. Eng. J.* 298 (2016) 44–54.
- [18] S. Hariharan, M. Werner, M. Hanchen, M. Mazzotti, Dissolution of dehydroxylated lizardite at flue gas conditions: II. Kinetic modeling, *Chem. Eng. J.* 241 (2014) 314–326.
- [19] M. Werner, S. Hariharan, D. Zingaretti, R. Baciocchi, M. Mazzotti, Dissolution of dehydroxylated lizardite at flue gas conditions: I. Experimental study, *Chem. Eng. J.* 241 (2014) 301–313.
- [20] E. Benhelal, M.I. Rashid, M.S. Rayson, J.D. Prigge, S. Molloy, G.F. Brent, A. Cote, M. Stockenhuber, E.M. Kennedy, Study on mineral carbonation of heat activated lizardite at pilot and laboratory scale, *J. CO<sub>2</sub> Util.* 26 (2018) 230–238.
- [21] E. Benhelal, M.I. Rashid, M.S. Rayson, G.F. Brent, T. Oliver, M. Stockenhuber,



- E.M. Kennedy, Direct aqueous carbonation of heat activated serpentine: Discovery of undesirable side reactions reducing process efficiency, *Appl Energy* 242 (2019) 1369–1382.
- [22] F. Farhang, T.K. Oliver, M.S. Rayson, G.F. Brent, T.S. Molloy, M. Stockenhuber, E.M. Kennedy, Dissolution of heat activated serpentine for CO<sub>2</sub> sequestration: The effect of silica precipitation at different temperature and pH values, *J. CO<sub>2</sub> Util.* 30 (2019) 123–129.
- [23] T.K. Oliver, F. Farhang, T.W. Hodgins, M.S. Rayson, G.F. Brent, T.S. Molloy, M. Stockenhuber, E.M. Kennedy, CO<sub>2</sub> capture modeling using heat-activated serpentine slurries, *Energy Fuel* 33 (2019) 1753–1766.
- [24] S.E. Ashbrook, D.M. Dawson, NMR spectroscopy of minerals and allied materials, *Nuc. Magn. Reson.* 45 (2016) 1–52.
- [25] R.D. Balucan, E.M. Kennedy, J.F. Mackie, B.Z. Dlugogorski, Optimization of antigorite heat pre-treatment via kinetic modeling of the dehydroxylation reaction for CO<sub>2</sub> mineralization, *Greenh. Gases* 1 (2011) 294–304.
- [26] B.Z. Dlugogorski, R.D. Balucan, Dehydroxylation of serpentine minerals: Implications for mineral carbonation, *Renew. Sust. Energy Rev.* 31 (2014) 353–367.
- [27] R.D. Balucan, B.Z. Dlugogorski, Thermal Activation of Antigorite for Mineralization of CO<sub>2</sub>, *Environ. Sci. Technol.* 47 (2013) 182–190.
- [28] M.S. Liu, G. Gadikota, Chemo-morphological coupling during serpentine heat treatment for carbon mineralization, *Fuel* 227 (2018) 379–385.
- [29] A.V.G. Chizmeshya, M.J. McKelvy, G.H. Wolf, R.W. Carpenter, D.A. Gormley, J.R. Diefenbacher, R. Marzke, Enhancing the atomic-level understanding of CO<sub>2</sub> mineral sequestration mechanisms via advanced computational modeling, *Arizona State Univ., Tempe, AZ (United States)*, 2006, pp. Medium: ED.
- [30] M.J. McKelvy, A.V.G. Chizmeshya, J. Diefenbacher, H. Bearat, G. Wolf, Exploration of the role of heat activation in enhancing serpentine carbon sequestration reactions, *Environ. Sci. Technol.* 38 (2004) 6897–6903.
- [31] M. Magi, E. Lippmaa, A. Samoson, G. Engelhardt, A.R. Grimmer, Solid-state high-resolution Si-29 chemical-shifts in silicates, *J. Phys. Chem-Us* 88 (1984) 1518–1522.
- [32] A. Bloise, M. Catalano, E. Barrese, A.F. Gualtieri, N.B. Gandolfi, S. Capella, E. Belluso, TG/DSC study of the thermal behaviour of hazardous mineral fibres, *J. Therm. Anal. Calorim.* 123 (2016) 2225–2239.
- [33] A. Cattaneo, A.F. Gualtieri, G. Artioli, Kinetic study of the dehydroxylation of chrysotile asbestos with temperature by in situ XRPD, *Phys. Chem. Miner.* 30 (2003) 177–183.
- [34] A.F. Gualtieri, C. Giacobbe, C. Viti, The dehydroxylation of serpentine group minerals, *Am. Mineral.* 97 (2012) 666–680.
- [35] A.F. Gualtieri, A. Tartaglia, Thermal decomposition of asbestos and recycling in traditional ceramics, *J. Eur. Ceram. Soc.* 20 (2000) 1409–1418.
- [36] R. Kusiorowski, T. Zaremba, J. Piotrowski, J. Adamek, Thermal decomposition of different types of asbestos, *J. Therm. Anal. Calorim.* 109 (2012) 693–704.
- [37] C. Viti, Serpentine minerals discrimination by thermal analysis, *Am. Mineral.* 95 (2010) 631–638.
- [38] P.A. Candela, C.D. Crummett, D.J. Earnest, M.R. Frank, A.G. Wylie, Low-pressure decomposition of chrysotile as a function of time and temperature, *Am. Mineral.* 92 (2007) 1704–1713.
- [39] S.W. Zhou, Y.G. Wei, B. Li, B.Z. Ma, C.Y. Wang, H. Wang, Kinetics study on the dehydroxylation and phase transformation of Mg<sub>3</sub>Si<sub>2</sub>O<sub>5</sub>(OH)<sub>4</sub>, *J. Alloy. Compd.* 713 (2017) 180–186.
- [40] K.J.D. Mackenzie, R.H. Meinhold, Thermal-reactions of chrysotile revisited - a Si-29 and Mg-25 Mas Nmr-study, *Am. Mineral.* 79 (1994) 43–50.
- [41] N. Zulumyan, A. Isahakyan, H. Beglaryan, S. Melikyan, A study of thermal decomposition of antigorite from dunite and lizardite from peridotite, *J. Therm. Anal. Calorim.* 131 (2018) 1201–1211.
- [42] M. Ghoorah, B.Z. Dlugogorski, H.C. Oskierski, E.M. Kennedy, Study of thermally conditioned and weak acid-treated serpentinites for mineralisation of carbon dioxide, *Miner. Eng.* 59 (2014) 17–30.
- [43] W. Ashraf, J. Olek, Elucidating the accelerated carbonation products of calcium silicates using multi-technique approach, *J. CO<sub>2</sub> Util.* 23 (2018) 61–74.
- [44] J.L. Cui, E.L. Sesti, J.K. Moore, D.E. Giammar, S.E. Hayes, Evidence from Si-29 solid-state nuclear magnetic resonance of dissolution reactions of forsterite, *Environ. Eng. Sci.* 33 (2016) 799–805.
- [45] M.C. Davis, W.J. Brouwer, D.J. Wesolowski, L.M. Anovitz, A.S. Lipton, K.T. Mueller, Magnesium silicate dissolution investigated by Si-29 MAS, H-1-Si-29 CPMAS, Mg-25 QCPMG, and H-1-Mg-25 CP QCPMG NMR, *PPCP* 11 (2009) 7013–7021.
- [46] K. Kosuge, K. Shimada, A. Tsunashima, Micropore formation by acid treatment of antigorite, *Chem. Mater.* 7 (1995) 2241–2246.
- [47] J.H. Kwak, J.Z. Hu, D.W. Hoyt, J.A. Sears, C.M. Wang, K.M. Rosso, A.R. Felmy, Metal carbonation of forsterite in supercritical CO<sub>2</sub> and H<sub>2</sub>O using solid state <sup>29</sup>Si, <sup>13</sup>C NMR spectroscopy, *J. Phys. Chem. C* 114 (2010) 4126–4134.
- [48] K.A. Smith, R.J. Kirkpatrick, E. Oldfield, D.M. Henderson, High-resolution Si-29 nuclear magnetic-resonance spectroscopic study of rock-forming silicates, *Am. Mineral.* 68 (1983) 1206–1215.
- [49] M.R. Hansen, H.J. Jakobsen, J. Skibsted, Si-29 chemical shift anisotropies in calcium silicates from high-field Si-29 MAS NMR spectroscopy, *Inorg. Chem.* 42 (2003) 2368–2377.
- [50] P.F. Barron, P. Slade, R.L. Frost, Solid-state Si-29 spin-lattice relaxation in several 2–1 phyllosilicate minerals, *J. Phys. Chem-Us* 89 (1985) 3305–3310.
- [51] J.V. Smith, C.S. Blackwell, Nuclear magnetic-resonance of silica polymorphs, *Nature* 303 (1983) 223–225.
- [52] C.A. Fyfe, G.C. Gobbi, J. Klinowski, J.M. Thomas, S. Ramdas, Resolving crystallographically distinct tetrahedral sites in silicalite and Zsm-5 by solid-state Nmr, *Nature* 296 (1982) 530–533.
- [53] S. Leonardelli, L. Facchini, C. Fretigny, P. Touge, A.P. Legrand, Silicon-29 NMR study of silica, *J. Am. Chem. Soc.* 114 (1992) 6412–6418.
- [54] S.M. Chemtob, G.R. Rossman, J.F. Stebbins, Natural hydrous amorphous silica: Quantitation of network speciation and hydroxyl content by Si-29 MAS NMR and vibrational spectroscopy, *Am. Mineral.* 97 (2012) 203–211.
- [55] T. Ida, M. Ando, H. Toraya, Extended pseudo-Voigt function for approximating the Voigt profile, *J. Appl. Crystallogr.* 33 (2000) 1311–1316.
- [56] D. Hrsak, G. Sucik, L. Lazic, The thermophysical properties of serpentine, *Metalurgija* 47 (2008) 29–31.
- [57] G.W. Brindley, R. Hayami, Mechanism of Formation of Forsterite and Enstatite from Serpentine, *Mineral Mag J M Soc* 35 (1965) 189–1000.
- [58] G.W. Brindley, J. Zussman, A structural study of the thermal transformation of serpentine minerals to forsterite, *Am. Mineral.* 42 (1957) 461–474.
- [59] T. Zaremba, A. Krzakala, J. Piotrowski, D. Garczorz, Study on the thermal decomposition of chrysotile asbestos, *J. Therm. Anal. Calorim.* 101 (2010) 479–485.
- [60] H. Bearat, M.J. McKelvy, A.V.G. Chizmeshya, D. Gormley, R. Nunez, R.W. Carpenter, K. Squires, G.H. Wolf, Carbon sequestration via aqueous olivine mineral carbonation: Role of passivating layer formation, *Environ. Sci. Technol.* 40 (2006) 4802–4808.
- [61] O.S. Pokrovsky, J. Schott, Forsterite surface composition in aqueous solutions: A combined potentiometric, electrokinetic, and spectroscopic approach, *Geochim. Cosmochim. Ac.* 64 (2000) 3299–3312.
- [62] O.S. Pokrovsky, J. Schott, Kinetics and mechanism of forsterite dissolution at 25 degrees C and pH from 1 to 12, *Geochim. Cosmochim. Ac.* 64 (2000) 3313–3325.
- [63] J. Cui, E.L. Sesti, J.K. Moore, D.E. Giammar, S.E. Hayes, Evidence from <sup>29</sup>Si solid-state nuclear magnetic resonance of dissolution reactions of forsterite, *Environ. Eng. Sci.* 33 (2016) 799–805.
- [64] S. Hariharan, M. Mazzotti, Kinetics of flue gas CO<sub>2</sub> mineralization processes using partially dehydroxylated lizardite, *Chem. Eng. J.* 324 (2017) 397–413.
- [65] K. Maher, N.C. Johnson, A. Jackson, L.N. Lammers, A.B. Torchinsky, K.L. Weaver, D.K. Bird, G.E. Brown, A spatially resolved surface kinetic model for forsterite dissolution, *Geochim. Cosmochim. Ac.* 174 (2016) 313–334.
- [66] R.J. Kirkpatrick, D. Howell, B.L. Phillips, X.D. Cong, E. Ito, A. Navrotsky, Mas Nmr spectroscopic study of Mg<sub>2</sub>SiO<sub>3</sub> with the perovskite structure, *Am. Mineral.* 76 (1991) 673–676.
- [67] J.J. Li, M. Hitch, Mechanical activation of magnesium silicates for mineral carbonation, a review, *Miner. Eng.* 128 (2018) 69–83.
- [68] T.C. Alex, R. Kumar, S.K. Roy, S.P. Mehrotra, Mechanical activation of Al-oxy-hydroxide minerals-a review, *Min. Proc. Ext. Met. Rev.* 37 (2016) 1–26.
- [69] A.H.A. Park, L.S. Fan, CO<sub>2</sub> mineral sequestration: physically activated dissolution of serpentine and pH swing process, *Chem. Eng. Sci.* 59 (2004) 5241–5247.
- [70] G. Rim, D. Wang, M. Rayson, G. Brent, A.-H.A. Park, Investigation on abrasion versus fragmentation of the Si-rich passivation layer for enhanced carbon mineralization via CO<sub>2</sub> partial pressure swing, *Ind. Eng. Chem. Res.* 59 (2020) 6517–6531.
- [71] J.J. Li, M. Hitch, Characterization of the microstructure of mechanically-activated olivine using X-ray diffraction pattern analysis, *Miner. Eng.* 86 (2016) 24–33.
- [72] S. Atashin, J.Z. Wen, R.A. Varin, Investigation of milling energy input on structural variations of processed olivine powders for CO<sub>2</sub> sequestration, *J. Alloy. Compd.* 618 (2015) 555–561.
- [73] D.J. Kim, H.S. Chung, Effect of grinding on the structure and chemical extraction of metals from serpentine, *Particul. Sci. Technol.* 20 (2002) 159–168.
- [74] Q.W. Zhang, K. Sugiyama, F. Saito, Enhancement of acid extraction of magnesium and silicon from serpentine by mechanochemical treatment, *Hydrometallurgy* 45 (1997) 323–331.
- [75] E. Benhelal, M.I. Rashid, M.S. Rayson, T.K. Oliver, G. Brent, M. Stockenhuber, E.M. Kennedy, “ACEME”: Synthesis and characterization of reactive silica residues from two stage mineral carbonation Process, *Environ. Prog. Sustain* 38 (2019).